This article was downloaded by: *[Oak Ridge National Laboratory]*
On: *28 May 2009*
Access details: *Access Details: [subscription number 909492212]*
Publisher *Taylor & Francis*
Informa Ltd Registered in England and Wales Registered Number: 1072954 Registered office: Mortimer House, 37-41 Mortimer Street, London W1T 3JH, UK

Dekker Encyclopedia of Nanoscience and Nanotechnology, Second Edition
Publication details, including instructions for authors and subscription information:
http://www.informaworld.com/smpp/title~content=t908795069

Electron Microscopy at Very High Resolution

Klaus van Benthem [ab]; Stephen J. Pennycook [c]
[a] Center for Nanophase Materials Sciences, Oak Ridge National Laboratory, Oak Ridge, Tennessee, U.S.A. [b] Department of Chemical Engineering and Materials Science, University of California-Davis, Davis, California, U.S.A. [c] Materials Science and Technology Division, Oak Ridge National Laboratory, Oak Ridge, Tennessee, U.S.A.

Online Publication Date: 25 March 2009

To cite this Section van Benthem, Klaus and Pennycook, Stephen J.(2009)'Electron Microscopy at Very High Resolution',Dekker Encyclopedia of Nanoscience and Nanotechnology, Second Edition,1:1,1217 — 1229

PLEASE SCROLL DOWN FOR ARTICLE

Full terms and conditions of use: http://www.informaworld.com/terms-and-conditions-of-access.pdf

This article may be used for research, teaching and private study purposes. Any substantial or systematic reproduction, re-distribution, re-selling, loan or sub-licensing, systematic supply or distribution in any form to anyone is expressly forbidden.

The publisher does not give any warranty express or implied or make any representation that the contents will be complete or accurate or up to date. The accuracy of any instructions, formulae and drug doses should be independently verified with primary sources. The publisher shall not be liable for any loss, actions, claims, proceedings, demand or costs or damages whatsoever or howsoever caused arising directly or indirectly in connection with or arising out of the use of this material.

Electron Microscopy at Very High Resolution

Klaus van Benthem
Center for Nanophase Materials Sciences, Oak Ridge National Laboratory, Oak Ridge, Tennessee, U.S.A., and Department of Chemical Engineering and Materials Science, University of California–Davis, Davis, California, U.S.A.

Stephen J. Pennycook
Materials Science and Technology Division, Oak Ridge National Laboratory, Oak Ridge, Tennessee, U.S.A.

Abstract
Transmission electron microscopy (TEM) is one of the most frequently used tools for the characterization of nanomaterials. Aberration-correction has revolutionized the field of electron microscopy and now equipment is commercially available providing sub-Ångström resolution and single atom sensitivity for atomic, electronic, and chemical structure analyses. In this entry, aberration-corrected scanning transmission electron microscopy and related techniques are reviewed in the framework of nanomaterials sciences. Three examples from the areas of catalysis, hydrogen storage, and nanoscale thin films, are used to demonstrate experimental capabilities and current resolution limits.

Downloaded By: [Oak Ridge National Laboratory] At: 19:44 28 May 2009

INTRODUCTION

The characterization of structure and electronic properties of materials is a key issue in modern nanotechnology. Electron microscopy techniques, especially transmission electron microscopy (TEM), are probably the most important tools for the investigation of nanomaterials since many properties can be directly accessed with very high spatial resolution.[1,2] The Royal Swedish Academy of Sciences named the electron microscope as "*one of the most important inventions*" of the 20th century.[3] Ever since the invention of the electron microscope in 1932,[4] technical advances have brought higher and higher resolution limits all the way to the ultimate limit for materials sciences: the imaging and identification of a single isolated atom. This development in increasing the spatial resolution for materials sciences is illustrated in Fig. 1. Already in 1936, it was recognized by Scherzer that lens aberrations occur in electron optical round lenses as a result of physics rather than purely due to imperfections,[5] hence limiting the achievable resolution orders of magnitude apart from the electron's wavelength. In his famous lecture entitled "*There's Plenty of Room at the Bottom,*" Feynman directly addressed the development of electron microscopes by asking "*Is there no way to make the electron microscope more powerful*?"[6] He suggested to break axial symmetries to overcome spherical aberrations and, thus, improve the resolution limits so that one could "*see individual atoms distinctly.*" Even though first designs of aberration-correctors already existed,[7] it was not until the advance of fast computers that aberration-correction became suitable for the electron microscope. Tuning and focusing correction elements for electron optics requires the alignment of many multipole lenses with accuracies of the order of 10^{-7}, resulting in a parameter space with more than 40 dimensions.

Today, aberration-correction is successfully applied to both TEM and scanning transmission electron microscopy (STEM), and enables the discrimination of two objects separated by less than 1 Å with both techniques. In addition, the high spatial resolution can be combined with spectroscopy techniques to determine local chemical compositions and electronic structures. Therefore, TEM and STEM are invaluable tools for modern nanomaterials research and provide structural and chemical information with unprecedented detail and sensitivity.

In the following, basic concepts of TEM and different techniques for nanocharacterization will be reviewed. Emphasis will be laid on aberration-correction in STEM. Afterwards, different examples from nanomaterials research will be reviewed, which could only be obtained through the application of aberration-corrected STEM. Finally, an outlook to future developments in TEM/STEM in connection to nanomaterials sciences and technology will be offered.

Transmission Electron Microscopy

The main focus of this entry lies on scanning transmission electron microscopy, in which a fine electron probe is scanned across the sample and signals provided by transmitted electrons are collected serially as a function of position on the sample. In contrast to STEM, conventional TEM uses a parallel illumination

Dekker Encyclopedia of Nanoscience and Nanotechnology, Second Edition DOI: 10.1081/E-ENN2-120043634
Copyright © 2009 by Taylor & Francis. All rights reserved.

Downloaded By: [Oak Ridge National Laboratory] At: 19:44 28 May 2009

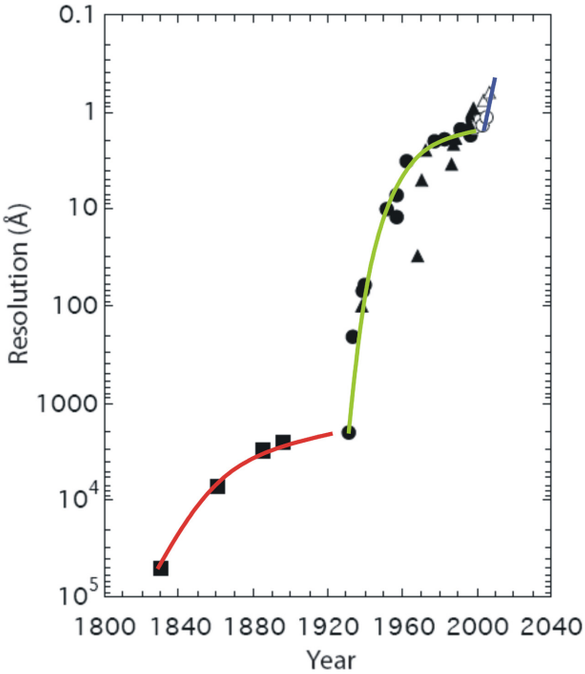

Fig. 1 The evolution of spatial resolution in microscopy since the early 1800s. Squares represent light microscopy, circles TEM, triangles STEM. Solid symbols refer to results obtained before aberration-correction, while open symbols denote studies after correction. Red, green, and blue lines, respectively, have been added to show overall trends. *Source*: Figure created from Ref.[8].

of the electron transparent specimens. For the coherent electron beam conditions in TEM, contrast is mainly achieved through the use of apertures in the back focal plane of the objective lens to select or interfere diffracted beams, referred to respectively as diffraction contrast or phase contrast imaging.[1] Figure 2 shows a sketch of the electron ray diagrams for STEM and TEM operation modes and compares the essential optical elements in both instruments for one picture element, i.e. image pixel. As can be inferred from Fig. 2, the bright field STEM and TEM ray diagrams are equivalent when read in opposite directions of electron propagation.[1] This equivalence is often referred to as the theory of reciprocity, which was formulated for light optics by Stokes, Lorentz, Helmholtz, and others in the 19th century.[9] The principle of reciprocity in the context of electron wave optics is based on time-reversal symmetry of the electron propagation process. The STEM collector aperture β_{STEM} is, therefore, equivalent to the TEM condenser aperture α_{TEM} while the objective aperture $\alpha_{STEM} = \beta_{TEM}$ remains the same. For clarification, apertures passed by the electron beam before interaction with the sample are denoted with angles α, while post-specimen apertures are called β. Note, however, in a combined TEM/STEM instrument the STEM objective (i.e. probe-forming) aperture is usually the same aperture used as condenser aperture in the TEM mode. The difference in the two operating conditions is that in STEM, the image pixels are recorded serially while in TEM they are all acquired at once. It is important to recognize that when identical apertures $\alpha_{STEM} = \beta_{TEM}$ and $\beta_{STEM} = \alpha_{TEM}$ are used, and provided that β_{STEM} is coherently and β_{TEM} is incoherently illuminated, the principle of reciprocity results in identical image contrast for bright field STEM and TEM.[1]

In an STEM instrument, electrons are accelerated from a source and focused into a small probe onto the specimen by a set of condenser lenses and an objective lens. The objective aperture limits the maximum angle under which electrons contribute to the electron probe, which is scanned across the sample by a set of scan coils.

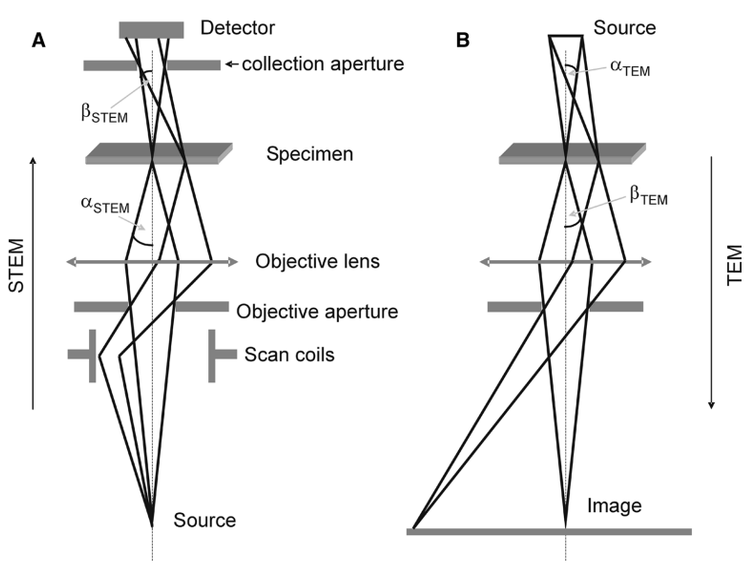

Fig. 2 Theorem of reciprocity between (A) STEM and (B) TEM in terms of electron ray diagrams connecting the intermediate source and image. *Source*: From Ref.[1].

Downloaded By: [Oak Ridge National Laboratory] At: 19:44 28 May 2009

Images are formed by recording electrons transmitted by the specimen as a function of probe position. Electrons scattered into high-angles are recorded with an annular detector. The cross-section for electrons scattered into high angles over a large angular range is roughly proportional to the squared atomic number of the scattering element.[1] For large enough scattering angles, coherent effects between, e.g., atomic columns average out. Hence, the scattering process itself can be considered purely incoherent, which bypasses the phase problem that complicates interpretation of conventional high-resolution TEM using phase contrast imaging. High-angle annular dark field (HAADF) imaging is often referred to as *Z*-contrast imaging because of the atomic number dependence of the scattering cross-section. Consequently, the HAADF technique is most sensitive to heavy elements, and images provide a high degree of chemical information in addition to structural details.[10]

Those electrons scattered into small angles can be collected "*on-axis*" by a bright field detector, or they can be analyzed with respect to their kinetic energy to form electron energy-loss spectra to investigate inelastic scattering events. In addition, secondary electron detectors, energy-dispersive X-ray detectors, cathodoluminescence detectors, etc. can also be attached to the microscope. Consequently, STEM provides the simultaneous acquisition of multiple different image and spectroscopy signals while scanning the electron probe across the specimen or pointing it directly onto different defect structures, such as, for instance, point defects, grain boundaries, or heterophase interfaces.[10] Figure 3A shows a schematic drawing of the main components of a dedicated STEM instrument. As an example, Fig. 3B is a picture of the VG Microscopes HB603 U dedicated STEM operated at 300 keV accelerating voltage, which is located at Oak Ridge National Laboratory.

The spatial resolution of an STEM experiment is determined by the diameter of the electron probe. Therefore, the probe formation is the critical aspect determining interaction volumes inside the sample. To increase the spatial resolution, aberration-correctors have recently been developed to overcome limitations due to lens imperfections and aberrations. In the following section, some basics of the concepts for aberration-correction will be reviewed.

Lens aberrations

Aberration-correction is most likely the most exciting recent development in electron optics and microscopy. Ideal lenses focus a point source to a single image point, as sketched in Fig. 4A. Scherzer, however, first recognized that every rotationally symmetric lens will always suffer from both spherical and chromatic aberrations.[5] Spherical aberrations cause electrons traveling at higher angles to the optical axis to be focused more strongly than those at smaller angles (cf. Fig. 4B). Chromatic aberrations describe the spread in focus of a lens dependent on the kinetic energy spread of the electron wave (Fig. 4B). Consequently, both types of lens aberrations lead to a blurring of the electron beam in the back focal plane and, hence, a degradation of the spatial resolution. The practical limit to the achievable spatial resolution in modern electron microscopes is determined by these lens aberrations and instrument instabilities to about 50 times the electron wavelength λ.

The aberration is an error in the optical path length between the actual wave front and the perfect sphere, and is commonly expressed as a Taylor expansion in angle θ. When ignoring all non-rotationally symmetric

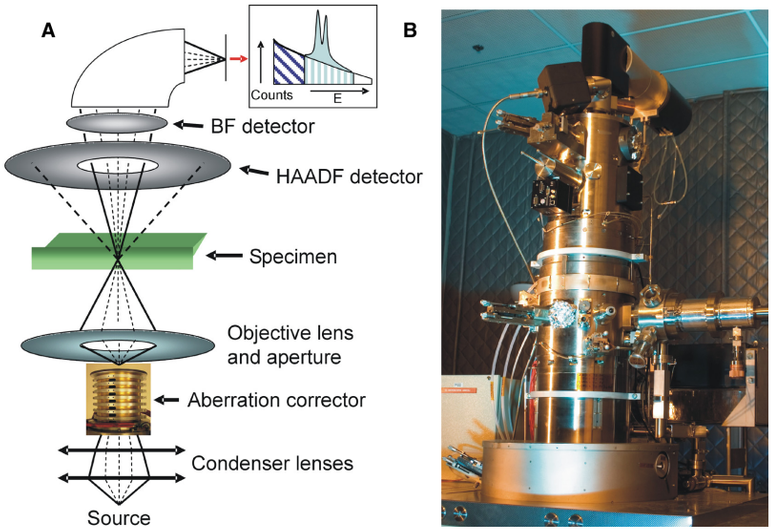

Fig. 3 (A) Schematic drawing of the main components of an aberration-corrected scanning transmission electron microscope. The geometric setup allows simultaneous recording of different detector signals. (B) Picture of the Oak Ridge VG Microscopes HB603 U dedicated STEM.

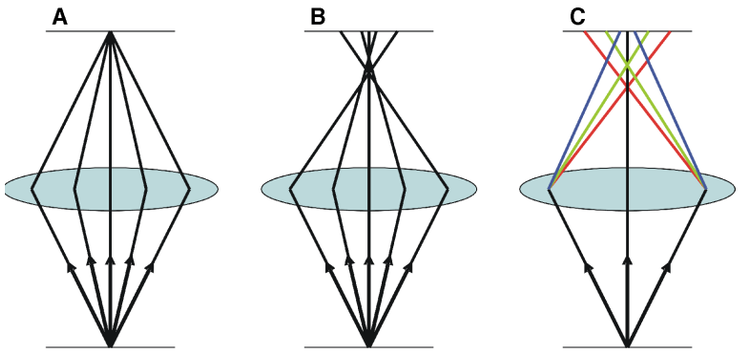

Fig. 4 Schematic drawing of main lens aberrations. (A) A perfect lens focuses a point source to a single image point. (B) Geometric aberrations such as the spherical aberration bring electron rays at different angles to different focus points. The chromatic aberration (C) focuses the electron beam at different positions as a function of energy blur. *Source*: Adapted and reprinted, with permission, from Ref.[10].

aberrations, the aberration function $X(\theta)$ becomes

$$X(\theta) = \frac{1}{2}\Delta f\theta^2 + \frac{1}{4}C_3\theta^4 + \frac{1}{6}C_5\theta^6 + \frac{1}{8}C_7\theta^8 + \cdots, \quad (1)$$

where Δf is the defocus, $C_3 = C_s$, C_5, and C_7 are the coefficients of third-, fifth-, and seventh-order spherical aberrations, respectively. For round magnetic lenses, these coefficients are all positive and have dimensions of length. At first, the order of the aberration coefficients seems counter-intuitive to Eq. (1). However, geometric aberrations lead the electron rays at different angles towards the different focus points along the optical axis, causing a lateral displacement in the Gaussian focal plane. The lateral displacements are proportional to the gradient of the aberration function $grad_\theta X(\theta)$.[11] Therefore, C_s is often referred to as a third-order spherical aberration.

Similar notations as used in Eq. (1) can be used for non-round aberrations, such as astigmatism, by introducing the dependence on the azimuthal angle. The description of general lens imperfection to fifth order would need 25 aberration coefficients to be included in the expression of the aberration function.[12,13] Fortunately, most of these coefficients are small in round lenses and can be kept small by suitable lens designs and microscope column alignments.

Aberration-correctors

In practice, every optical lens exhibits aberrations. The underlying principle used by aberration-correctors is to generate an identical but negative aberration coefficient, which cancels out with the one introduced by the actual lens itself. The fundamental strategy to achieve this has been laid out by Scherzer in 1947 when he proposed to break rotational symmetry to eliminate spherical and chromatic aberrations.[7] Consequently, non-round optical elements, so-called multipoles, have been used to facilitate aberration-correction for round lenses. At the time of writing, there are two main types of aberration-correctors commercially available: the quadrupole–octupole corrector from Nion[12–14] and the round-lens-hexapole corrector from CEOS.[15,16] Both types of correctors consist of either octupoles or hexapoles as correction elements, and quadrupoles or round lenses as steering elements for the electron trajectories inside the corrector. The two different designs have certain advantages and disadvantages when compared with each other. A discussion of the two different strategies is well beyond the scope of this entry. However, it should be noted that the round-lens-hexapole design can not only be used for the probe-forming lenses in STEM, but also was initially introduced to the imaging optics of high-resolution TEM instruments to achieve sub-Ångström resolution.[17,18] In STEM, direct imaging of a crystal lattice with sub-Ångström resolution has been achieved initially with the quadrupole–octupole corrector design (see Fig. 5).[19,20] Similar results were reproduced shortly thereafter with the hexapole corrected STEM.[18]

Effects of aberration-correction

The initial goal of all efforts to correct lens aberrations in electron microscopy was to increase the spatial resolution, i.e. to decrease the electron probe diameter in the case of STEM. That this goal has been achieved is demonstrated with today's sub-Ångström spatial resolution imaging conditions (see Figs. 1 and 5). However, in STEM aberration-correction provides two additional effects: single atom sensitivity[21] and drastically increased depth sensitivity.[20,22]

Figure 6 shows calculated electron probe profiles before and after aberration-correction. For both simulations, the number of electrons, i.e. the electron beam current, is conserved. It becomes immediately evident that not only the probe diameter becomes significantly smaller, but at the same time the intensity increases dramatically. In HAADF imaging, the signal scales with the square power of the reciprocal probe diameter, while the background scales with the square power of the diameter itself. Therefore, the strongly

Downloaded By: [Oak Ridge National Laboratory] At: 19:44 28 May 2009

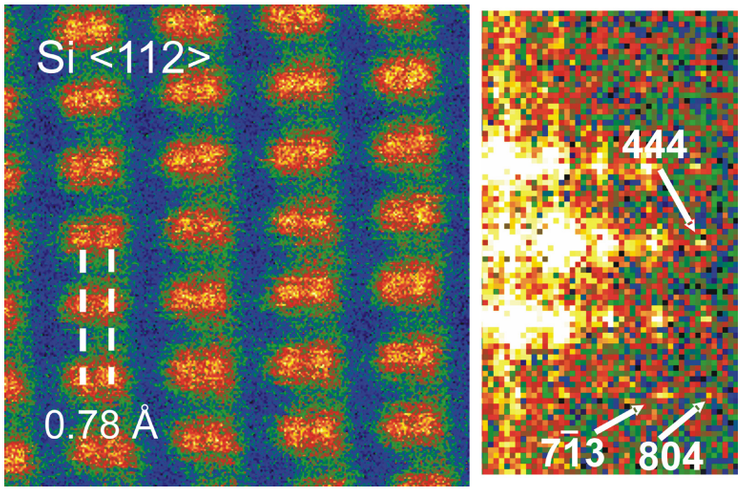

Fig. 5 HAADF image directly recorded from a silicon single crystal, which was oriented with its <112> direction parallel to the optical axis. Columns of Si atoms only 0.78 Å apart from each other were clearly resolved. The right panel shows a part of the Fourier transform of the same image revealing information transfer to 0.61 Å.[22] *Source*: Figure reproduced with permission from Ref.[19].

increased beam current density after aberration-correction conveys higher sensitivity for annular dark field imaging, which enables single atom sensitivity in annular dark field images.[21]

The depth of field T in STEM can be expressed as the quotient of lateral spatial resolution $\delta_s = 0.61^*\lambda/\alpha$ and the probe-forming angle α[1]

$$T = \frac{\delta_s}{\alpha} = 0.61\frac{\lambda}{\alpha^2} \tag{2}$$

Equation (2) shows that the availability of larger illumination angles because aberration-correction decreases the depth of field much faster than it improves the lateral resolution. The major consequence of the smaller depth of field is that only very thin slices of the specimen come into focus at a time. Hence, a through-focal series acquisition of images can provide optical sectioning of the sample along the optical axis in a manner comparable to confocal optical microscopy.[22] Such depth sectioning techniques have recently been established[20,23,24] and represent an additional avenue to tilt-series tomography[25,26] to deduce three-dimensional information from TEM samples.

The achievable three-dimensional spatial resolution, however, is highly anisotropic. As discussed above, aberration-corrected STEM has demonstrated sub-Ångström resolution in the lateral, i.e. in-plane directions. For the 300 keV VG HB603 U STEM at Oak Ridge, the depth of focus following Eq. (2) ranges around 3–4 nm.[22–24] Two atoms vertically displaced by the depth of focus T reveal total image intensity as shown in Fig. 7, which is, because of the incoherent nature of ADF imaging, a superposition of the contributions from each individual atom. Figure 7 demonstrates that in this case, the atoms cannot be discriminated using the depth-sectioning technique. For vertical distances equal to $1.75T$, the resulting image intensity plateaus, which is formally equivalent to a resolution criterion by Sparrow.[27,28] Both atoms can clearly be

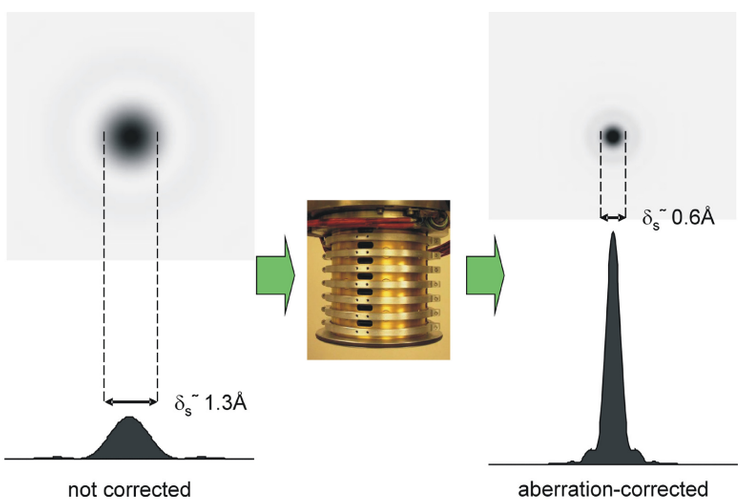

Fig. 6 Simulated images and intensity line profiles of the electron probe before and after aberration-correction. The number of electrons is identical in both cases. *Source*: Adapted with permission from Ref.[10].

Downloaded By: [Oak Ridge National Laboratory] At: 19:44 28 May 2009

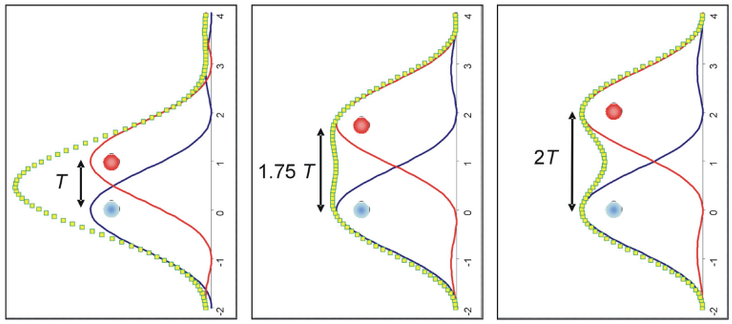

Fig. 7 Sketch of two isolated atoms vertically separated by 1×, 1.75×, and 2× the depth of field *T*. At the position of each atom, a simulated vertical probe profile is plotted. The dotted line is a superposition of the two corresponding profiles and represents the resulting image intensity as a function of defocus. *Source*: Adapted from Ref.[24] with permission from Elsevier.

discriminated along the optical axis for vertical displacements of 2*T*, for which the resulting image intensity reveals a contrast variation of about 20% between the atoms. Therefore, this condition has been chosen as a criterion for vertical resolution. It is equivalent to the lateral resolution criterion formulated by Lord Raleigh in that, in the absence of aberrations, one atom is placed at the first zero of the diffracted intensity of the other.[11,28,29]

Examples and applications of single atom sensitivity in STEM imaging and depth sectioning techniques, both of which are direct consequences of aberration-correction, will be discussed further.

MICROSCOPY OF NANOMATERIALS

In the following sections, three applications of aberration-corrected STEM to functional nanomaterials, results obtained from activated carbon fibers, catalyst nanoparticles, and alternate gate dielectrics, will be reviewed.

Activated Carbon Fibers for Hydrogen Storage

Nanostructured carbon materials, such as carbon fibers, are lightweight inexpensive materials, which exhibit hydrogen storage capabilities.[30–33] Physisorption of H_2 on nanoporous carbon, although significant at cryogenic temperatures, is weak at room temperatures[30] and does not satisfy the current goals established by the US Department of Energy. However, on physical activation with CO_2[31] or doping with catalyst materials,[32] the hydrogen uptake can be enhanced when compared with unmodified carbons.

Recently, it was shown that significant enhancements of H_2 adsorption can be achieved at room temperature and 20 bar for activated carbon fibers (ACF) modified with Pd catalyst particles.[33] To control such processes in greater detail, and to further enhance the hydrogen uptake capacity, it is necessary to understand the fundamental atomistic mechanisms of metal-assisted hydrogen storage on nanostructured carbon fibers, and in particular, on how processing conditions affect the microstructure of Pd-doped activated carbon fibers.[34]

The following results were obtained from a sample processed at Clemson University.[35] An isotropic pitch precursor was mixed with about 1% Pd salt before melt-spinning. The traditional subsequent carbonization and activation processes were combined into a single-stage process of *direct carbonization and activation* in pure CO_2, and samples with various levels of burn-off were generated.[35] The particular material used for the results presented is characterized by a burn-off level of 40%. Further details of the materials processing and the effect on materials properties can be found in Refs.[34,35]. The hydrogen storage characteristics are not the subject of this entry and are reported elsewhere.[33] Details on the microscopy results reviewed in the following are the object of a separate publication.[36]

As described above, ADF images are very sensitive to heavy elements since the scattering cross-section is roughly proportional to the squared atomic number of the illuminated species. However, bright field (BF) images, which are very sensitive to light elements in the sample, can be recorded simultaneously (see Fig. 3). Aberration-correction in STEM leads to ''slower'' oscillations of the phase contrast transfer function so that larger BF detectors can be used.[37] This directly results into BF images with enhanced signal when compared with the uncorrected case, which, according to the theorem of reciprocity, are equivalent to phase-contrast images. The simultaneous acquisition of ADF and BF images with pixel-to-pixel correlation at very high resolution becomes a very powerful tool for the investigation of carbon microstructures in the presence of catalytic Pd particles.[36]

Figure 8 shows a pair of ADF and BF images, which were acquired with an aberration-corrected VG Microscopes HB603 U STEM operated at 300 keV. The microscope is equipped with a Nion third-order aberration-corrector (cf. Fig. 1). Bright spot-like contrasts in the ADF image represent small Pd clusters and, in many cases, even single isolated Pd atoms

Downloaded By: [Oak Ridge National Laboratory] At: 19:44 28 May 2009

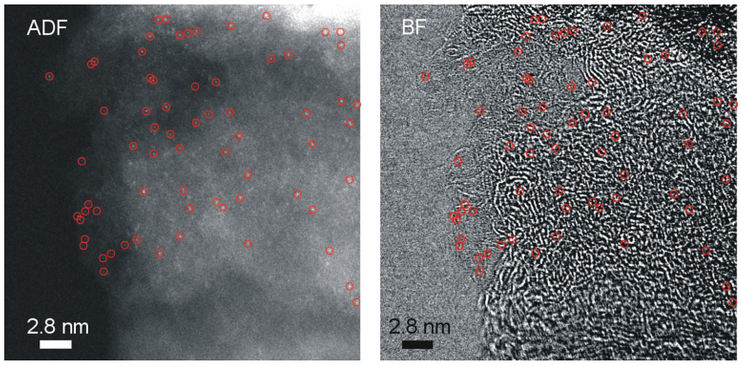

Fig. 8 Simultaneously acquired pair of ADF and BF images using the 300 keV aberration corrected dedicated STEM. The frames have pixel-to-pixel correlation, so that the location of single Pd atoms in the ADF images (encircled) can be superimposed on the BF image, which reveals the local carbon microstructure. *Source*: Image adapted from Ref.[36].

distributed throughout the carbon microstructure. Through-focal series acquisition of ADF images was used to confirm that the observed bright regions are due to single Pd atoms.[37] Pd atoms became very mobile due to illumination with the electron beam and could in many cases not be imaged at the exact same location in a subsequently acquired frame but at a nearby position.

The simultaneously acquired BF image clearly reveals the carbon microstructure exhibiting graphene sheets in various different orientations. It is evident that the carbon fiber material is somewhat disordered on a larger length scale. However, some structural ordering with parallel but bent graphene layers can be observed. The overall contrast in the ADF image varies in steps from dark on the left to lighter gray on the right side, indicating different specimen thicknesses in the direction parallel to the electron beam. In the upper right corner, the ADF image shows a bright contrast region, which appears significantly dark in the BF image. This contrast is due to a larger Pd particle extending into the field of view when this set of images was acquired.

Figure 9 shows three magnified areas extracted from the BF image shown in Fig. 8. In Fig. 9A, one Pd atom is located within a highly disordered, probably amorphous region, while a second Pd atom is terminating one graphene sheet located in between two others. Figure 9B shows a configuration in which a Pd atom is surrounded by concentric graphene sheets. A third configuration was observed in which Pd atoms are located in between two quasi-parallel sheets, which reveal slightly increased distances at and close to the Pd atom location. Such bending of atomic planes and the corresponding local straining reveals nanosized voids or pores inside the carbon microstructure correlated with the presence of single catalyst atoms. Previous investigations[38–40] indicate that nanosized pores are highly effective for hydrogen storage so that the configurations identified by STEM (Fig. 9) may represent local storage sites for atomic hydrogen after a spillover process,[41] encouraged by the presence of the metal catalyst. Such fundamental understanding of atomic-scale processes accessible by high-resolution STEM correlated with materials functionality, such as increased hydrogen gas uptake, can lead to more effective design of future storage materials.

Catalyst Particles

In the previous section, it was shown that single isolated atoms can be detected and laterally localized

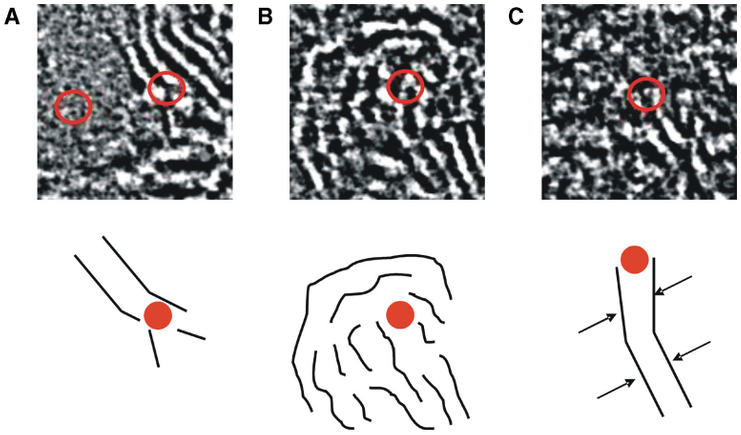

Fig. 9 Three different areas extracted from the BF image in Fig. 8 with the positions of single Pd atoms transferred from the corresponding ADF images encircled. In the schematics underneath, the location of white BF contrasts is sketched as black lines, while the Pd atoms are marked by filled circles. *Source*: BF intensities are discussed in detail in Ref.[36], from which this figure was adapted.

Downloaded By: [Oak Ridge National Laboratory] At: 19:44 28 May 2009

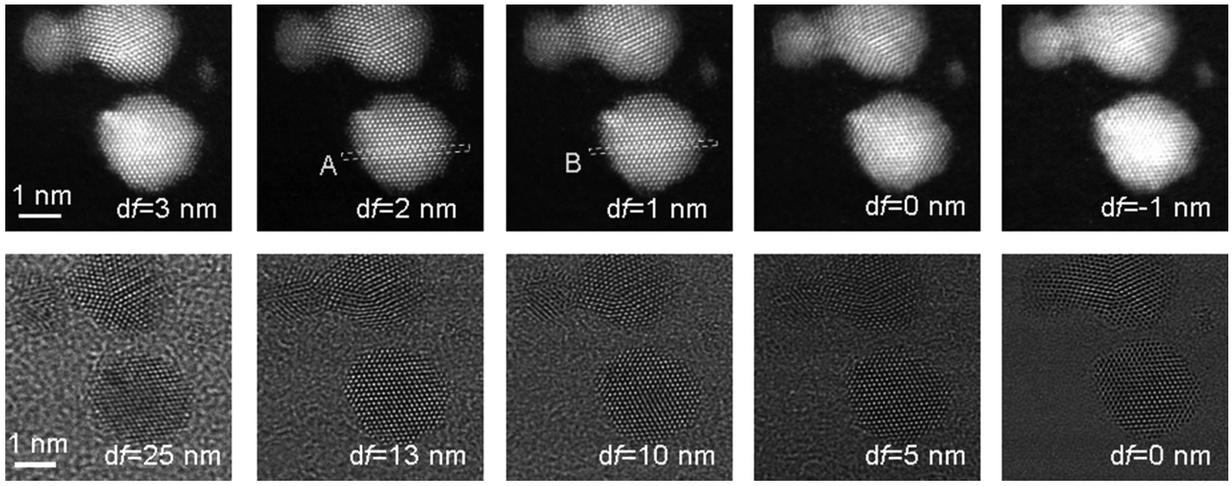

Fig. 10 ADF (top row) and BF (lower row) images extracted from a through-focal series of Au nanoclusters supported by an amorphous carbon film. The defocus (df) at which the images were taken is listed. *Source*: Figure reproduced from Ref.[42] with permission from Materials Research Society.

Downloaded By: [Oak Ridge National Laboratory] At: 19:44 28 May 2009

using aberration-corrected STEM. However, often times image quantification is desired to determine the absolute number of atoms forming, for instance, a catalyst particle. Since STEM typically provides a projection view of the investigated sample, the quantification of image contrast could in principle be used to determine specimen thickness.

Figure 10 shows a number of frames extracted from a through-focal series of simultaneously acquired ADF (upper row) and BF images (lower row) recorded from Au catalyst particles supported by an amorphous carbon film. The micrographs show four gold particles. The ADF image clearly exhibits lattice contrast for the crystalline particles while the carbon support film is almost invisible due to the Z-dependence of the scattering cross-section and, therefore, the large contrast differences. The corresponding bright-field images, however, clearly show the typical speckle pattern for amorphous carbon, whose contrast depends on the defocus value during image acquisition. Furthermore, the BF images also reveal lattice information of the Au clusters but with different contrast when compared with the ADF images.[1] The BF intensities change with defocus and even show contrast reversal, which is a typical feature of phase contrast imaging.[1] However, in this case the contrast inversion in the area of the amorphous carbon support film was used to calibrate the defocus scale.[42] Owing to the incoherent conditions for large inner detector angles, no reversal of contrast occurs for any defocus value in ADF imaging.

The ADF micrographs in Fig. 10 clearly exhibit regions with spot-like bright contrasts, which extend over multiple image pixels, and therefore represent single Au atoms in the vicinity of the larger Au clusters (see, e.g., frames labeled df = 2 nm and df = 3 nm). In Fig. 11, two intensity line profiles A and B are plotted as a function of relative distance across one of the Au particles. The direction and exact location from which these profiles were extracted are marked in Fig. 10. Arrows in Fig. 11A highlight three different locations where minimal but identical image intensities of about 350 counts/pixel above the background level can be observed. These intensities represent single Au atoms.

Complimentary ADF image simulations were performed using parameters as determined by the aberration-corrector to calculate quantitative image intensities as a function of specimen thickness, i.e. number of Au atoms in a column. For the calculations an Au crystal was oriented with the <111> zone-axis parallel to the incoming beam direction, resembling the experimental conditions as observed for the lower Au cluster in Fig. 10. It was found that the incoherent ADF signal is *linear* with the number of Au atoms for columns containing up to 6 atoms (see Fig. 12). Beyond 6 atoms, the ADF signal flattens out and channeling effects complicate the image quantification.

Based on the calculated calibration curve in Fig. 12, ADF image intensities were analyzed quantitatively. For each atomic column, the number of Au atoms along the electron beam direction was assigned. The results for line profile B are included in Fig. 11B. The anomalous background between the atomic columns could result from the so-called Stobbs factor.[43] Effects of chromatic aberrations or increased Debye–Waller factors due to a lower melting point of nanocrystalline Au clusters did not contribute to this background according to the image simulations.[42]

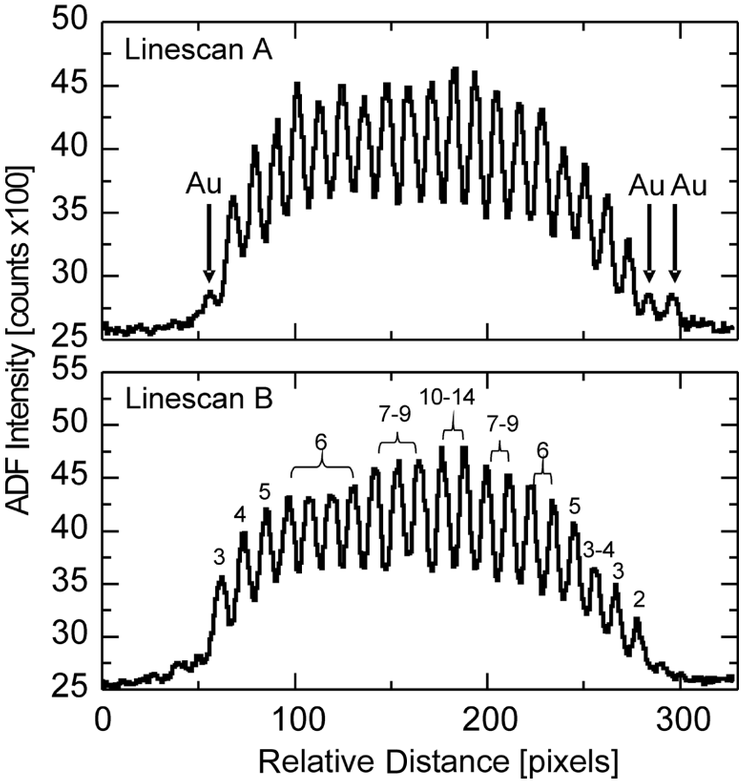

Fig. 11 ADF intensity line profiles as extracted from the areas marked in Fig. 10. The net counts per single Au atoms were extracted from linescan labeled A, and the number of Au atoms in each column for the profile labeled B was assigned. *Source*: Original data are published in Ref.[42]. Figure reproduced from Ref.[42] with permission from Materials Research Society.

The number of atoms in each individual column of an atomically resolved catalyst particle can thus be determined with very high accuracy, which, in the case discussed here, is ±1 atom for columns containing up to 6 atoms, and ±2–4 atoms for columns extending 2–4 nm along the beam direction. For the interpretation of catalytic activities, however, the true three-dimensional shape of the particle and its faceting is

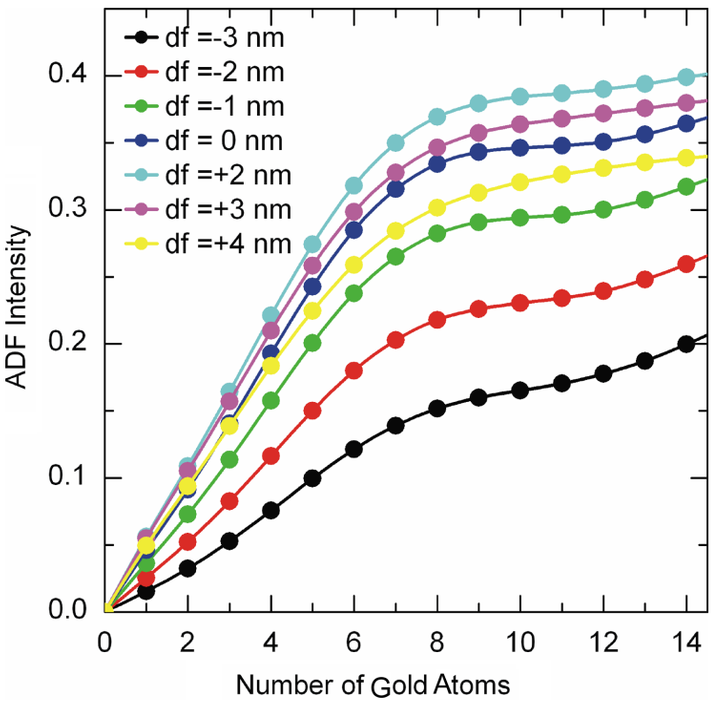

Fig. 12 Calculated fractional ADF intensities for different defocus values as a function of the number of Au atoms along the beam direction. The ADF intensity scales linearly with the number of atoms up to a thickness of 6–7 atoms.[42] *Source*: Figure reproduced from Ref.[42] with permission from Materials Research Society.

Downloaded By: [Oak Ridge National Laboratory] At: 19:44 28 May 2009

Downloaded By: [Oak Ridge National Laboratory] At: 19:44 28 May 2009

of critical importance. Such aspects, though at smaller resolution, can be addressed by tilt-series electron tomography of single catalyst particles.[26] In a recent study, Huang et al. have combined ADF image quantification as described earlier with statistical data for crystal shapes to determine the true three-dimensional shape of Au nanoparticles[44] and how many Au atoms they contain. In the future, a combination of these techniques might reveal more detailed information about faceting and shaping of nanoparticles with single atom accuracy.

Nanoscale Thin Films

It is well recognized that the macroscopic properties of polycrystalline or composite materials are determined to a large extent by their internal two-dimensional defect structures such as heterophase interfaces and grain boundaries.[45] Most structural and functional ceramics, for example, exhibit intergranular films with thicknesses around 1 nm (see, e.g., Ref.[46] and references therein). Composite materials provide their functionality through thin films with thicknesses in the nanometer regime. Very prominent examples are complex oxide structures exhibiting colossal magnetoresistance[47] or superconductivity properties.[48] Other examples include high-*k* dielectric films present in many semiconductor devices. Here, shrinking dimensions[49,50] demand material replacements to maintain device performance even though critical structures have dimensions of only a few atoms.[51,52] It is, therefore, of utmost importance to gain a fundamental understanding of interface structures and, hence, thin film properties.

HfO_2 is a prominent candidate as a replacement for SiO_2 as a high-*k* dielectric in semiconductor device structures. For the study reviewed in the following, 3 nm of HfO_2 were grown on the (100) surface of a silicon substrate using atomic layer deposition at 320°C. Afterwards, the thin film was capped with polycrystalline silicon by chemical vapor deposition techniques and rapid thermally annealed at 950°C in N_2 atmosphere for 30s. Cross-sectional TEM samples of the interface structure were prepared by mechanical wet-polishing[22] until electron transparency was reached. Figure 13 shows a pair of ADF and BF images simultaneously recorded from the interface structure. The TEM sample was oriented with the <110> direction in the silicon substrate parallel to the optical axis. Owing to the relatively high atomic number of Hf ($Z = 72$), the crystalline HfO_2 film appears with bright contrast in the ADF image. The typical silicon "dumbbell" spacing of 1.36 Å in this orientation is clearly observable in the ADF image. The BF image reveals an 8 Å wide amorphous interlayer between the HfO_2 thin film and the substrate. This interlayer was found to be a sub-stoichiometric silicon oxide.[53,54]

A through-focal series acquisition of ADF images revealed that within the SiO_x interlayer, bright spot-like features come into focus in various different areas at different focus settings. Figure 14 shows nine frames extracted from a through-focal series. It was found that these contrast features are due to single isolated Hf atoms embedded inside the interlayer,[22] which can hence be located laterally with sub-Å precision and vertically with better than 0.5 nm accuracy owing to the focal increment of 0.5 nm/frame during the data acquisition.[22,24] According to the increased depth sensitivity discussed earlier, the recorded stack of images from the through-focal series acquisition contains three-dimensional information about the interface structure. A 3D representation of the imaging data was created by surface and volume rendering techniques[22] and is shown in Fig. 15. The HfO_2 film is represented by bold yellow color. Columns of Si atoms can be observed in addition to five representative Hf atoms located in the interlayer, which was not color-coded. Overall, a concentration of 1.40 ± 0.11 atoms/nm^3 was found inside the interlayer.[22] A systematic investigation of the growth and annealing conditions during the interface formation revealed that the concentration of Hf atoms in the interlayer critically depends on the

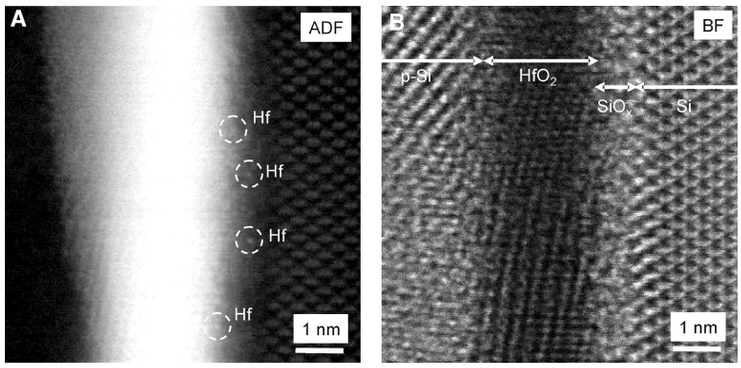

Fig. 13 Simultaneously acquired ADF (A) and BF (B) images of the alternate gate stack consisting of a HfO_2 layer deposited on a silicon substrate. The BF image reveals an amorphous interlayer formed between the alternate gate dielectric and the substrate. The ADF image exposes single Hf atoms within this interlayer. *Source*: Reprinted with permission from Ref.[42].

Downloaded By: [Oak Ridge National Laboratory] At: 19:44 28 May 2009

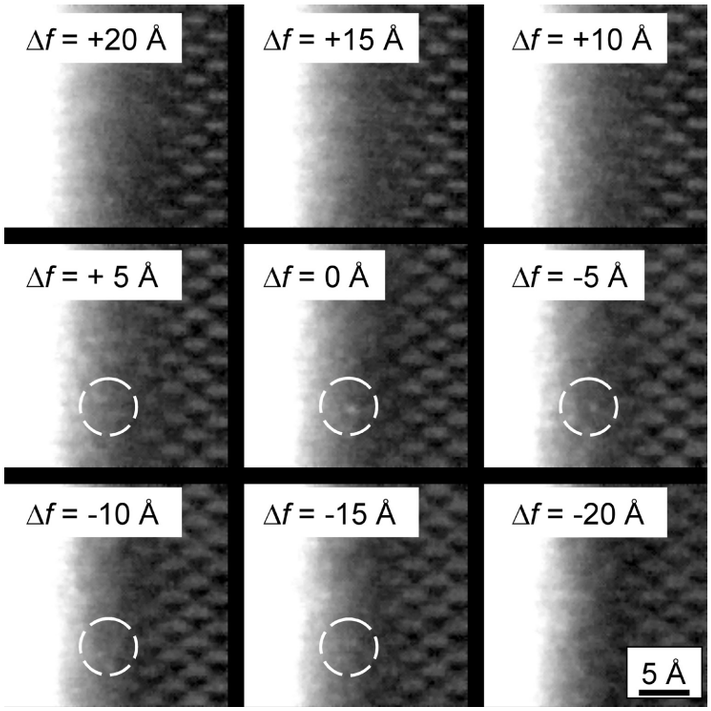

Fig. 14 ADF images extracted from a through-focal series showing spot-like bright contrasts representing single Hf atoms coming into focus at different locations.[24,55] *Source*: Figure reproduced from Ref.[42] with permission from Elsevier.

quality, i.e. stoichiometry, of the silicon oxide before the annealing process[54] and the oxygen affinity of the alternative high-*k* material.[54,56] Hf atoms diffuse into the suboxide interlayer during the rapid thermal annealing process owing to oxygen vacancy formation.[54,56] This ultimately creates states in the silicon band gap and can thus affect electron mobilities along or leakage across the gate channel.[56,57] The detection, identification and location of individual stray atoms and a fundamental understanding of their impact on the macroscopic materials properties is a critical aspect for the design and future application of functional nanomaterials.

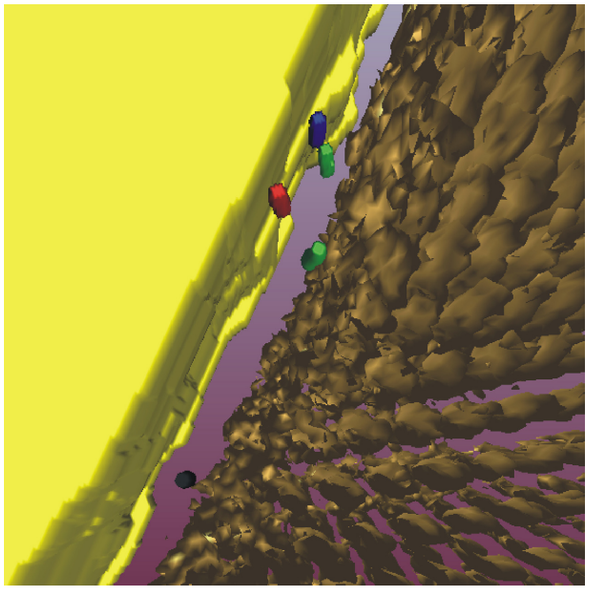

Fig. 15 3D reconstruction of the $HfO_2/SiO_x/Si$ interface structure. The HfO_2 film is represented by bold yellow on the left while columns of Si atoms can (gold color) can be observed on the right. Five Hf atoms are reconstructed with black, green, blue, and red colors inside the interlayer (not color-coded). *Source*: Reprinted with permission from Ref.[42].

CONCLUSIONS AND FUTURE DIRECTIONS

In this entry, it was illustrated how aberration-corrected STEM can be applied for the characterization of a wide variety of nanostructured materials. The STEM represents an invaluable tool for the structural and chemical investigation of nanostructures using a variety of different imaging and spectroscopy tools. Aberration-correction has revolutionized electron microscopy by enabling the formation of electron probes with diameters well below 1 Å and enhanced depth sensitivity by reducing the depth of field. A resulting consequence is that STEM data can no longer be interpreted as a simple two-dimensional projection of a three-dimensional structure, but provides three-dimensional information with the ultimate sensitivity down to one single atom. Three different materials systems have been discussed here for which STEM techniques provided insights into atomic and electronic structures with heretofore unprecedented detail. Even

though many of the unanswered questions in the field of materials sciences can be addressed with lower resolution imaging capabilities than reported here, it is the sensitivity down to a single atom that is ultimately important and critical.

The availability of atomic resolution imaging and spectroscopy in combination with single atom sensitivities in all three dimensions stimulates a renewed interest in *in situ* capabilities. If it were possible to maintain the resolution limits on heating or cooling of the sample or changing the gas pressure and atmosphere during the experiments, new fundamental insights could be gained to understand critical processes in functional materials on the atomic length scale in their anticipated working environments. Such advances in electron microscopy will probably lead to an over-achievement of Feynman's request for a "*better electron microscope.*"

Downloaded By: [Oak Ridge National Laboratory] At: 19:44 28 May 2009

ACKNOWLEDGMENTS

Discussions with A.R. Lupini, A.Y. Borisevich, M.F. Chisholm, M.P. Oxley, Y. Peng, N.D. Gallego, S.N. Rashkeev, and S.T. Pantelides are gratefully acknowledged. This work was funded by the U.S. Department of Energy, Division of Scientific User Facilities (KvB) and Division of Materials Sciences and Engineering (SJP). Partial financial funding from the Alexander-von-Humboldt Foundation (KvB) is gratefully acknowledged.

REFERENCES

1. Reimer, L. *Transmission Electron Microscopy*, 4th Ed.; Springer: Berlin, Heidelberg, New York, 1997.
2. Williams, D.B.; Carter, C.B. *Transmission Electron Microscopy*; Plenum Press: New York, USA, 1996 and London, UK.
3. http://nobelprize.org/nobel_prizes/physics/laureates/1986/press.html; (accessed January 2008).
4. Knoll, M.; Ruska, E. Das Elektronenmikroskop. Z. Physik **1932**, *78*, 318–339.
5. Scherzer, O. Über einige Fehler von Elektonenlinsen. Zeit. Phys. **1936**, *101*, 593–603.
6. Feynman, R.P. There's plenty of room at the bottom. Eng. Sci. **1960**, *23*, 22–36.
7. Scherzer, O. Sphärische und kromatische Korrektur von Elektronen-Linsen. Optik **1947**, *2*, 114–132.
8. Rose, H. Correction of aberrations, a promising means for improving the spatial and energy resolution of energy-filtering electron microscopes. Ultramicroscopy **1994**, *56*, 11–25.
9. Potton, R.J. Reciprocity in optics. Rep. Prog. Phys. **2004**, *67*, 717–754.
10. Varela, M.; Lupini, A.R.; van Benthem, K.; Borisevich, A.Y.; Chisholm, M.F.; Shibata, N.; Abe, E.; Pennycook, S.J. Materials characterization in the aberration-corrected scanning transmission electron microscope. Ann. Rev. Mater. Res. **2005**, *35*, 539–569.
11. Born, M.; Wolf, E. *Principles of Optics*; Pergamon Press: Oxford, UK, 1980.
12. Dellby, N.; Krivanek, O.L.; Nellist, P.D.; Batson, P.E.; Lupini, A.R. Progress in aberration-corrected scanning transmission electron microscopy. J. Electron Microscopy **2001**, *50*, 177–185.
13. Krivanek, O.L.; Dellby, N.; Lupini, A.R. Towards sub-angstrom electron beams. Ultramicroscopy **1999**, *78*, 1–11.
14. www.nion.com (accessed January 2008).
15. Rose, H. Outline of a sherically corrected semiaplanatic medium-voltage transmission electron microscope. Optik **1990**, *85*, 19–24.
16. www.ceos-gmbh.de (accessed January 2008).
17. Haider, M.; Rose, H.; Uhlemann, S.; Schwan, E.; Kabius, B.; Urban, K. A spherical-aberration-corrected 200 kV transmission electron microscope. Ultramicroscopy **1998**, *75*, 53–60.
18. O'Keefe, M.A.; Allard, L.F.; Blom, D.A. HRTEM imaging of atoms at sub-Ångstrom resolution. J. Electron Microscopy **2005**, *54*, 169–180.
19. Nellist, P.D.; Chisholm, M.F.; Dellby, N.; Krivanek, O.L.; Murfitt, M.F.; Szilagyi, Z.S.; Lupini, A.R.; Borisevich, A.Y.; Sides, W.H.; Pennycook, S.J. Direct sub-Ångstrom imaging of a crystal lattice. Science **2004**, *305*, 1741.
20. Borisevich, A.Y.; Lupini, A.R.; Travaglini, S.; Pennycook, S.J. Depth sectioning of aligned crystals with the aberration-corrected scanning transmission electron microscope. J. Electron Microscopy **2006**, *55*, 7–12.
21. Wang, S.W.; Borisevich, A.Y.; Rashkeev, S.N.; Glazoff, M.V.; Sohlberg, K.; Pennycook, S.J.; Pantelides, S.T. Dopants adsorbed as single atoms prevent degradation of catalysts. Nature Mater. **2004**, *3*, 143–146.
22. van Benthem, K.; Lupini, A.R.; Kim, M.; Baik, H.S.; Doh, S.J.; Lee, J.-H.; Oxley, M.P.; Findlay, S.D.; Allen, L.J.; Pennycook, S.J. Three-dimensional imaging of individual hafnium atoms inside a semiconductor device. Appl. Phys. Lett. **2005**, *87*, 034104.
23. Borisevich, A.Y.; Lupini, A.R.; Pennycook, S.J. Depth-sectioning with the aberration-corrected scanning transmission electron microscope. Proc. Natl. Acad. Sci. **2006**, *103*, 3044–3048.
24. van Benthem, K.; Lupini, A.R.; Oxley, M.P.; Findlay, S.D.; Allen, L.J.; Pennycook, S.J. Three dimensional ADF imaging of individual atoms by through-focal series scanning transmission electron microscopy. Ultramicroscopy **2006**, *106*, 1062–1068.
25. Midgley, P.A.; Weyland, M. 3D electron microscopy in the physical sciences: the development of Z-contrast and EFTEM tomography. Ultramicroscopy **2003**, *96*, 413–431.
26. Arslan, I.; Yates, T.J.V.; Browning, N.D.; Midgley, P.A. Science **2005**, *309*, 2195–2198.
27. Sparrow, C.M. Spectroscopic resolving power. Astrophys. J. **1916**, *44*, 76–86.
28. den Dekker, A.J.; von den Bos, A. Resolution: a survey. J. Opt. Soc. Am. A **1997**, *14*, 547–557.

29. Lord Raleigh Investigations in optics, with special reference to the spectroscope. Philos. Mag. **1879**, *8*, 261–274, 403–411, 477–486.
30. David, E. An overview of advanced materials for hydrogen storage. J. Mater. Process. Technol. **2005**, *162/163*, 169.
31. Panella, B.; Hirscher, M.; Roth, S. Hydrogen adsorption in different carbon nanostructures. Carbon **2005**, *43*, 2209–2214.
32. Anson, A.; Lafuente, E.; Urriolabeitia, E.; Navarro, R.; Benito, A.M.; Maser, W.; Martinez, M.T. Hydrogen capacity of palladium-loaded carbon materials. J. Phys. Chem. B **2006**, *110*, 6643–6648.
33. Contescu, C.I.; Gallego, N.C.; Wu, X.; Tekinalp, H.L.; Edie, D.D.; Baker, F.S. Extended abstract to CARBON '07, International Carbon Conference, Seattle, WA, USA, July 15–20, 2007.
34. Wu, X.; Gallego, N.C.; Contescu, C.I.; Tekinalp, H.; Bhat, V.; Baker, F.S.; Thies, M.C.; Edie, D.D. The effect of processing conditions on microstrcuture of Pd-containing activated carbon fibers. Carbon **2008**, *46*, 54–61.
35. Tekinalp, H.L.; Cervo, E.; Edie, D.D.; Thies, M.C.; Contescu, C.I. *Extended abstract to CARBON '07*, International Carbon Conference, Seattle, WA, USA, July 15–20, 2007.
36. van Benthem, K.; Pennycook, S.J.; Contescu, C.I.; Gallego, N.D. in preparation.
37. Lupini, A.R.; Rashkeev, S.N.; Varela, M.; Borisevich, A.Y.; Oxley, M.P.; van Benthem, K.; Peng, Y.; de Jonge, N.; Veith, G.M.; Chisholm, M.F.; Pennycook, S.J. Scanning transmission electron microscopy. In *Nanocharacterization*; Kirkland, A.I., Hutchinson, J.L., Eds.; Royal Society of Chemistry: London, UK, 2007.
38. de la Casa-Lillo, M.A.; Lamari-Darkrim, F.; Cazorla-Amorós, D.; Linares-Solano, A. Hydrogen storage in activated carbons and activated carbon fibers. J. Phys. Chem. B **2002**, *106*, 10,930–10,934.
39. Zhao, X.; Villar-Rodil, S.; Fletcher, A.J.; Thomas, K.M. Kinetic isotope effect for H_2 and D_2 quantum molecular sieving in adsorption/desorption on porous carbon materials. J. Phys. Chem. B **2006**, *110*, 9947–9955.
40. Aga, R.S.; Fu, C.L.; Krčmar, M.; Morris, J.R. Theoretical investigation of the effect of graphite interlayer spacing on hydrogen absorption. Phys. Rev. B **2007**, *76*, 165404.
41. Lueking, A.D.; Yang, R.T. Hydrogen spillover onto carbon: Inference of spillover hydrogen on optimization for hydrogen storage. Appl. Catal. A: General **2004**, *265*, 259–268.
42. van Benthem, K.; Peng, Y.; Pennycook, S.J. Tomographic imaging of nanocrystals vs aberration-corrected scanning transmission electron microscopy. Mat. Res. Soc. Symp. Proc. **2005**, *839*, 3–8.
43. Hÿtch, M.J.; Stobbs, W.M. Quantitative comparison of high-resolution TEM images and image simulations. Ultramicroscopy **1994**, *53*, 191–203.
44. Huang, B.; Wang, W.; Bates, M.; Zhuang, X. Three-dimensional super-resolution imaging by stochastic optical reconstruction microscopy. Science **2008:** DOI: 10.1126/science.1153529.
45. Sutton, A.P.; Balluffi, R.W. *Interfaces in Crystalline Materials*; Clarendon Press: Oxford, UK, 1996.
46. Hoffmann, M.J.; Petzow, G.; Eds. *Tailoring of Mechanical Properties of Si_3N_4 Ceramics*; NATO ASI Series E 267; Kluwer Acad. Publ.: Dordrecht, 1994.
47. Jin, S.; Tiefel, T.H.; McCormack, M.; Fastnacht, R.A.; Ramesh, R.; Chen, L.H. Thousandfold change in resistivity in magnetoresistive La-Ca-Mn-O films. Science **1994**, *264*, 413–415.
48. Triscone, J.-M.; Fischer, Ø. Rep. Superlattices of high-temperature superconductors: synthetically modulated structures, critical temperatures and vortex dynamics. Prog. Phys. **1997**, *60*, 1673–1721.
49. Moore, G. Cramming more components into integrated circuits. Electronics **1965**, 38.
50. Packan, P.A. Pushing the limits. Science **1999**, *285*, 2079–2081.
51. Semiconductor Industry Association. The National Technology Roadmap for Semiconductors 71-81, Sematech, Austin, TX, 1997.
52. Muller, D.A.; Sorsch, T.; Moccio, S.; Baumann, F.H.; Evans-Lutterodt, K.; Timp, G. The electronic structure at the atomic scale of ultra-thin gate oxides. Nature **1999**, *399*, 758–761.
53. van Benthem, K.; Rashkeev, S.N.; Pennycook, S.J. Atomic and electronic structure investigations of $HfO_2/SiO_2/Si$ gate stacks using aberration-corrected STEM. AIP Conf. Proc. **2005**, *788*, 79–84.
54. van Benthem, K.; Pennycook, S. Imaging and spectroscopy of defects in semiconductors using aberration-corrected STEM. Appl. Phys. A **2008** (in press).
55. Corrigendum to reference 23, in preparation.
56. Bersuker, G.; Park, C.S.; Barnett, J.; Lysaght, P.S.; Kirsch, P.D.; Young, C.D.; Choi, R.; Lee, B.H.; Foran, B.; van Benthem, K.; Pennycook, S.J.; Lenahan, P.M.; Ryan, J.T. The effect of interfacial layer properties on the performance of Hf-based gate stack devices. J. Appl. Phys. **2006**, *100*, 094108.
57. Rashkeev, S.N.; van Benthem, K.; Pantelides, S.T.; Pennycook, S.J. Single Hf atoms inside the ultrathin SiO_2 interlayer between an HfO_2 dielectric film and the Si substrate: How do they modify the interface? Microelectron. Eng. **2005**, *80*, 416–419.

BIBLIOGRAPHY

1. Peng, Y.; Oxley, M.P.; Lupini, A.R.; Chisholm, M.F.; Pennycook, S.J. Spatial resolution and information transfer in scanning transmission electron microscopy. Microsc. Microanal. **2008**, *14*, 36–47.

Downloaded By: [Oak Ridge National Laboratory] At: 19:44 28 May 2009